Manifestation of a non-Abelian Berry phase in a *p*-type semiconductor system

T. Li,[1] L. A. Yeoh,[1] A. Srinivasan,[1] O. Klochan,[1] D. A. Ritchie,[2] M. Y. Simmons,[3] O. P. Sushkov,[1] and A. R. Hamilton[1]

[1]*School of Physics, University of New South Wales, Sydney 2052, Australia*

[2]*Cavendish Laboratory, J. J. Thomson Avenue, Cambridge CB3 0HE, United Kingdom*

[3]*Centre for Quantum Computation and Communication Technology, School of Physics, University of New South Wales, Sydney NSW 2052, Australia*

(Received 5 October 2015; revised manuscript received 17 April 2016; published 17 May 2016; corrected 3 June 2016)

Gauge theories, while describing fundamental interactions in nature, also emerge in a wide variety of physical systems. Abelian gauge fields have been predicted and observed in a number of novel quantum many-body systems, topological insulators, ultracold atoms, and many others. However, the non-Abelian gauge field, while playing the most fundamental role in particle physics, up to now has remained a purely theoretical construction in many-body physics. In this paper, we report an observation of a non-Abelian gauge field in a spin-orbit coupled quantum system. The gauge field manifests itself in quantum magnetic oscillations of a hole doped two-dimensional (2D) GaAs heterostructure. Transport measurements were performed in tilted magnetic fields, where the effect of the emergent non-Abelian gauge field was controlled by the components of the magnetic field in the 2D plane.

DOI: 10.1103/PhysRevB.93.205424

I. INTRODUCTION

Gauge theories were originally conceived to describe elementary particles and their interactions [1,2]. The concept of the emergent gauge field is relevant to a wide class of quantum systems whose initial formulation has no apparent relationship to gauge fields. Such emergent gauge fields arise naturally in many geometrical contexts and the idea that physical systems can be classified according to their geometrical properties has become an overarching paradigm of modern physics. One example of an Abelian gauge theory in this context is the Berry phase [3], which is associated with the adiabatic evolution of a nondegenerate quantum state. The emergence of non-Abelian gauge fields in degenerate quantum systems was first theoretically proposed by Wilczek and Zee [4] shortly after the work of Berry.

While Abelian gauge fields have been observed in systems ranging from optical fibers [5] and semiconductor rings [6,7] to Bose condensates of ultracold atoms [8], signs of non-Abelian effects have so far only been observed in the nuclear quadrupole resonance of ^{35}Cl in a single crystal of sodium chlorate [9]. Non-Abelian gauge fields have been theoretically predicted in a number of many-body systems including fractional quantum Hall liquids [10], spin-orbit coupled systems [11,12], cuprate superconductors [13], and ensembles of ultracold atoms [14,15]. In spite of the theoretical excitement and great interest, all previous attempts to observe these fields were unsuccessful. This demonstrates the challenge involved in the experimental realization of emergent non-Abelian gauge fields.

The idea of our experiment is partially based on previous theoretical work by Arovas and Lyanda-Geller [11] as well as Murakami, Nagaosa, and Zhang [12] who proposed that effects relating to non-Abelian gauge fields must be pronounced in hole-doped zinc-blende semiconductors due to the strong spin-orbit coupling (SOC). In this context, the gauge fields are closely associated with spin dynamics along curved trajectories: Ref. [11] proposed the use of mesoscopic rings to bend the trajectory, while Ref. [12] suggested use of an external electric field for the same purpose. In this work, we use a two-dimensional (2D) GaAs hole-doped heterostructure in a relatively small (fraction of a Tesla) magnetic field applied perpendicular to the 2D plane to curve the hole trajectories. In addition, we apply an in-plane magnetic field ($B_\parallel \sim$ several Tesla), which allows us to control the magnitude of the spin-orbit coupling. The combination of the SOC and curved trajectories makes the non-Abelian gauge field observable. The perpendicular magnetic field gives rise to quantum magnetic oscillations which are influenced by non-Abelian spin dynamics. We measure the oscillations via the Shubnikov–de Haas (SdH) effect. The SdH effect has been measured previously in numerous experiments with 2D systems with strong spin-orbit interaction (see, e.g., Refs. [16,17]). However, in all previous studies, effects related to the non-Abelian Berry phase are negligible, and what is measured is simply the densities of the spin-split subbands. One needs very special conditions to distinguish between the Abelian and the non-Abelian Berry phases, it is necessary to tune independently the spin precession, the orbital dynamics, and the spin-orbit interaction. To do so in our experiment we use the following crucial points. (i) We can tune the spin-orbit coupling over a wide range using the in-plane field $B_\parallel$ while keeping the orbital dynamics fixed. (ii) We use a low-symmetry crystal with highly anisotropic coupling to $B_\parallel$, which allows us to control independently the Larmor and the spin precession frequencies. This is key to proving that the effects we observe cannot be due to Abelian physics, nor due to differences between data sets taken at different carrier densities, gate biases, or even from different samples. (iii) We use a device where we can minimize the undesirable Rashba interaction, allowing a simple analytic theory to explain the data. These three factors allow us to report the first observation of the non-Abelian gauge phase which was elusive for 30 years since its theoretical prediction.

The spin dynamics of a particle moving around a circle in momentum space used in Onsager quantization [18] is illustrated in Fig. 1. The three panels in this figure correspond to three qualitatively different situations: (a) spin dynamics being absent, (b) Abelian spin dynamics, and (c) non-Abelian spin dynamics. The spin (red arrows) is driven by a local

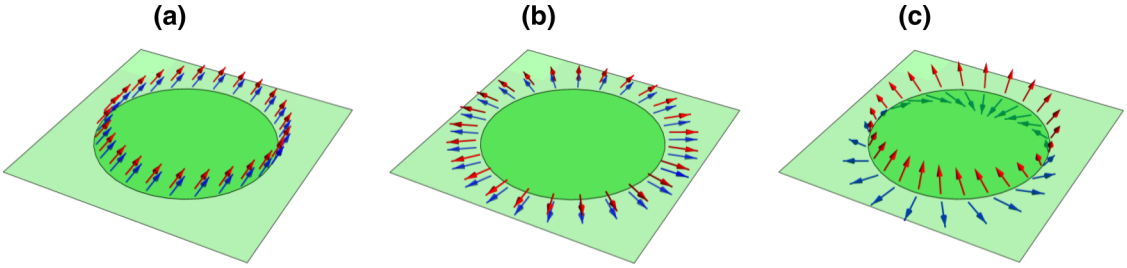

FIG. 1. Spin dynamics along the closed trajectory in momentum space (green circle) in three qualitatively different situations. The spin shown by red arrows is driven by a local effective magnetic field shown by blue arrows. (a) Absence of spin dynamics. This corresponds to the case of an electron moving within an external magnetic field in the absence of spin-orbit interaction. (b) Abelian spin dynamics. Spin is changing, but it remains parallel to the driving field $\boldsymbol{B}_{\rm eff} \propto \boldsymbol{k}$. (c) Non-Abelian spin dynamics. The spin is parallel to the vector sum of the driving field $\boldsymbol{B}_{\rm eff}$ and the non-Abelian gauge field.

effective magnetic field $\boldsymbol{B}_{\rm eff}$ (blue arrows), which is the sum of the external magnetic field $\boldsymbol{B}_{\rm ext}$ and the momentum-dependent spin-orbit field $\boldsymbol{B}_{\rm SOC}$. Figure 1(a) depicts the trajectory of a nonrelativistic electron in the absence of spin orbit. In this case, $\boldsymbol{B}_{\rm eff} = \boldsymbol{B}_{\rm ext}$ and the spin is simply aligned with the external field. Figure 1(b) illustrates the case of an ultrarelativistic Dirac electron, e.g., an electron in graphene or on the surface of a topological insulator. In this case, although spin is precessing, it remains aligned with the driving field which itself is parallel to the momentum $\boldsymbol{B}_{\rm eff} \approx \boldsymbol{B}_{\rm SOC} \propto \boldsymbol{k}$. The precession of spin around the orbit generates a geometric Berry phase (Abelian gauge field) which appears as the π-phase shift observed in magnetic oscillations [19,20]. The non-Abelian case addressed in this work is illustrated in Fig. 1(c). Here, the driving field $\boldsymbol{B}_{\rm eff}$ is not collinear with spin and the noncollinearity is proportional to the non-Abelian gauge field. Due to the non-Abelian spin dynamics, the particle acquires a matrix-valued phase equal to the circulation of the gauge field around the trajectory in momentum space. The phase manifests itself in quantum magnetic oscillations.

II. ORIGIN OF THE NON-ABELIAN GAUGE FIELD IN *p*-TYPE SYSTEMS

Holes in GaAs originate from atomic $p_{3/2}$ orbitals and hence possess an angular momentum $J = \frac{3}{2}$. The electric quadrupole interaction leads to strong coupling between the angular momentum $\boldsymbol{J}$ and the linear momentum $\boldsymbol{k}$, which is described by the Luttinger Hamiltonian [21]. The z confinement in a 2D heterostructure enforces quantization of $\boldsymbol{J}$ along the z axis. Therefore, a hole quantum state with a given in-plane momentum $\boldsymbol{k} = (k_x, k_y)$ splits into two doublets with $J_z = \pm\frac{3}{2}$ (heavy holes) and $J_z = \pm\frac{1}{2}$ (light holes). Since light holes lie significantly higher in energy, we shall only consider heavy holes for the low-energy dynamics.

The heavy-hole Kramers doublet can be described by an effective spin $s = \frac{1}{2}$, $|J_z = +\frac{3}{2}\rangle \equiv |\uparrow\rangle$, $|J_z = -\frac{3}{2}\rangle \equiv |\downarrow\rangle$. The Hamiltonian describing heavy holes consists of the kinetic energy, the Zeeman interaction, and the SOC, $H = H_K + H_Z + H_{\rm SOC}$:

$$H_K = \epsilon(\boldsymbol{k}), \quad H_Z = -\frac{\Delta}{2}\sigma_z\,, \quad \Delta = g\mu_B B_z,$$
$$H_{\rm SOC} \equiv -\boldsymbol{\beta}(\boldsymbol{k})\cdot\boldsymbol{\sigma} = -\frac{1}{2}\alpha[\sigma_+ B_- k_-^2 + \sigma_- B_+ k_+^2], \tag{1}$$

where $\boldsymbol{k} = -i\hbar\nabla - e\boldsymbol{A}$; $\sigma_\pm = \sigma_x \pm i\sigma_y$, $B_\pm = B_x \pm iB_y$, $k_\pm = k_x \pm ik_y$; $\boldsymbol{A}$ is the in-plane vector potential created by B_z, e is the elementary charge, σ_i are Pauli matrices describing the spin, μ_B is Bohr magneton, $g = g_{zz}$ is the effective g factor, and α is the SOC strength. Note that due to mixing between heavy-hole states the dispersion $\epsilon(k)$ can significantly differ from the simple quadratic form (see discussion in Appendix A). Note also that generally g and α depend on k, and in combination with nonquadratic dispersion $\epsilon(k)$ this dependence results in a very complex fan diagram of Landau levels. However, according to the Landau theory of normal Fermi liquids, this complexity is irrelevant to the problem we address. We do not need the full Landau level fan diagram. According to normal Fermi liquid theory, only the values of the parameters at the Fermi energy are relevant. This statement is very general, and even includes hole-hole Coulomb interaction effects. We will fit the experimental data to obtain the parameters g and α at $\epsilon = \epsilon_F$. A derivation of the spin-orbit interaction $H_{\rm SOC}$ is presented in Appendix A, although we shall make two comments here on its origin: (i) The spin-orbit coupling arises from a small mixing between heavy and light holes, where the mixing probability is 1%–2% (see Appendix A). (ii) The kinematic structure of $H_{\rm SOC}$ in Eq. (1) is dictated by the fact that the Pauli matrices $\sigma_\pm$ correspond to $\Delta J_z = \pm 3$.

If the perpendicular magnetic field is zero, $\boldsymbol{A} \propto B_z = 0$, then the hole trajectories are straight lines and $H_{\rm SOC}$ in Eq. (1) simply splits the doubly degenerate band ϵ_k into a pair of chiral bands. In presence of B_z, the hole trajectory forms a circle $\boldsymbol{k} = k(\cos\theta, \sin\theta)$. Semiclassically, using the wave-packet picture, the angle is $\theta = -\omega_c t$ (the sign corresponds to $B_z > 0$), where $\omega_c = e|B_z|/m$ is the cyclotron frequency and $m = k(\frac{d\epsilon}{dk})^{-1}$ is the effective cyclotron mass at the Fermi energy. The spin-orbit field $\boldsymbol{\beta}(\boldsymbol{k})$ varies along the trajectory. This variation can be removed by a local gauge transformation of the spinor wave function $\psi \to \psi' = g^{-1}(\boldsymbol{k})\psi$. Taking $g(\boldsymbol{k}) = e^{-i\theta\sigma_z}$ we gauge out the angle dependence of the SOC:

$$\boldsymbol{\beta}'(\boldsymbol{k})\cdot\boldsymbol{\sigma} = g^{-1}[\boldsymbol{\beta}\cdot\boldsymbol{\sigma}]g\,, \quad \boldsymbol{\beta}' = \alpha k^2 \boldsymbol{B}_\parallel\,. \tag{2}$$

Since our choice of $g(\boldsymbol{k})$ ensures that we perform a transformation to the corotating frame of the hole, it follows that $\boldsymbol{\beta}'$ does not vary along the trajectory. The gauge transformation results in the covariant derivative $\nabla \to \nabla - i\boldsymbol{\Omega}_{\boldsymbol{k}}$, where $\boldsymbol{\Omega}_{\boldsymbol{k}}$ is the non-Abelian gauge field possessing a vortex structure in

2D momentum space

$$\boldsymbol{\Omega_k} = ig^{-1}\nabla_{\boldsymbol{k}} g = \left(-\frac{k_y\sigma_z}{k^2}, \frac{k_x\sigma_z}{k^2}\right). \quad (3)$$

The field tensor corresponding to this gauge field is zero, $F_{\mu\nu} = \partial_\mu\Omega_\nu - \partial_\nu\Omega_\mu - i[\Omega_\mu,\Omega_\nu] = 0$. However, the gauge field has a nonzero circulation along the hole trajectory

$$\oint \boldsymbol{\Omega_k}\cdot\boldsymbol{dk} = 2\pi\sigma_z, \quad (4)$$

and this circulation reveals itself in quantum magnetic oscillations.

To understand quantum magnetic oscillations, we need to consider the impact of spin-orbit coupling upon the Landau level structure. For this analysis, we restrict ourselves to a semiclassical approximation, where the Landau levels are determined by the Onsager quantization condition. Consider a hole traversing the circular trajectory, where the hole is initially prepared in a polarization state $\psi(0)$. Under the combined action of $H_{\rm SOC}$ and H_Z spin will precess along the trajectory, as shown in Fig. 1(c). After a full cycle, the spin wave function is $\psi(2\pi) = U\psi(0)$, where $U \in {\rm SU}(2)$ is a unitary evolution matrix. In order to satisfy the semiclassical quantization condition, it is necessary for $\psi(0)$ to be an eigenvector of U, i.e., $\psi(2\pi) = e^{\pm i\Phi}\psi(0)$. Here, $e^{\pm i\Phi}$ are the complex-conjugate eigenvalues of U. Hence, depending on the spin state, an additional phase $\pm\Phi$ appears in the Onsager quantization condition due to spin dynamics.

III. MANIFESTATION OF NON-ABELIAN GAUGE FIELDS IN SHUBNIKOV-DE HAAS OSCILLATIONS

SdH oscillations in the resistivity are given by the usual Lifshitz-Kosevich formula [22]. Accounting for the additional phase Φ we obtain

$$\Delta\rho_{xx} = \rho_{xx}(B) - \rho_{xx}(0) = \mathcal{A}(B)\cos\Phi\cos\frac{\pi k_F^2}{e|B_z|}. \quad (5)$$

The amplitude factor depends on the hole scattering time τ, $\mathcal{A}(B) \propto e^{-\frac{\pi}{\omega_c\tau}}$. Spin dynamics enters only via the spin evolution phase factor ${\rm tr}U = 2\cos\Phi$. For the semiclassical approximation approach we assume large filling factors $\nu = \frac{k_F^2}{2e|B_z|} \gg 1$, hence, only the lowest harmonic of magnetic oscillations is taken into consideration.

The matrix phase U may be explicitly expressed as a path-ordered exponential which can be calculated using the gauge transformation from Eq. (2):

$$\begin{aligned} U &= \mathcal{P}\exp\left\{-\frac{i}{\omega_c}\oint\left[\boldsymbol{\beta}\cdot\boldsymbol{\sigma} + \frac{\Delta}{2}\sigma_z\right]d\theta\right\} \\ &= \exp\left\{i\oint\Omega_{\boldsymbol{k}}\cdot\boldsymbol{dk} - i\frac{2\pi}{\omega_c}\left[\boldsymbol{\beta}'\cdot\boldsymbol{\sigma} + \frac{\Delta}{2}\sigma_z\right]\right\}. \quad (6)\end{aligned}$$

Hence, using Eqs. (4) and (2) we find the prefactor in Eq. (5) for SdH oscillations $2\cos\Phi = {\rm tr}U$:

$$\Phi = \frac{2\pi}{\omega_c}\sqrt{\left(\omega_c - \frac{\Delta}{2}\right)^2 + \left|\alpha k_F^2\right|^2\left(B_x^2 + B_y^2\right)}. \quad (7)$$

Here, the ω_c term under the square root comes from the non-Abelian gauge field. It is worth noting that the effect of the gauge field is somewhat analogous to Thomas precession in special relativity [23]. As previously mentioned, the gauge field cannot be observed without the in-plane magnetic field. This is evident from Eq. (7): if $\boldsymbol{B}_\parallel = 0$ the gauge contribution is exactly 2π and hence the phase shift is determined only by the Zeeman splitting ${\rm tr}U = 2\cos(\pi\Delta/\omega_c)$. The Zeeman splitting with $\boldsymbol{B}_\parallel \neq 0$ is $\delta E_Z = \sqrt{(\frac{\Delta}{2})^2 + |\alpha k_F^2|^2(B_x^2 + B_y^2)}$. A naïve expectation for the spin accumulated phase would be $\Phi_{\rm naive} = 2\pi\delta E_Z/\omega_c$, but Eq. (7) is different from this. A seminaïve expectation would take into account the Abelian Berry phase φ_B on top of the Zeeman splitting. The phase φ_B is given by the first term of the square-root expansion in (7) in powers of ω_c, yielding

$$\Phi_{\rm AB} = \frac{2\pi\delta E_Z}{\omega_c} + \varphi_B = \frac{2\pi\delta E_Z}{\omega_c} - \frac{\pi\Delta}{\delta E_Z}. \quad (8)$$

The subscript "AB" in Φ stands for "Abelian Berry." The Abelian Berry phase approach provides a good description for magneto-oscillations in Dirac fermion systems [19,20], and for quantum interference in mesoscopic rings with strong spin-orbit coupling [6,7]. However, in our case, both the "naïve" $\Phi_{\rm naive}$ and the Abelian Berry phase $\Phi_{\rm AB}$ approach are inconsistent with the data.

IV. COMPARISON WITH EXPERIMENTAL DATA

In our experiments, the 2D hole system is formed in a 20-nm-wide symmetric GaAs quantum well, grown in a (311)A GaAs-$Al_{0.33}Ga_{0.67}As$ heterostructure as indicated in Fig. 2(a). Previous experiments on this system have shown that holes in a (311) oriented quantum well have a tensor g factor with an unusual off-diagonal term g_{xz} [24]. Although tilted field measurements revealed the presence of the g_{xz} term, no comparison of the Shubnikov–de Haas oscillations with theory was possible, as there was no theory available for 2D hole systems in tilted magnetic fields. We are now able to show that there is excellent qualitative agreement between the experimental data and the new theoretical model based on the non-Abelian gauge field.

We use the coordinates $x \parallel [\bar{2}33]$, $y \parallel [0\bar{1}1]$, $z \parallel [311]$ shown in Fig. 2(a). The gyromagnetic tensor is not diagonal in the x, y, and z axes, therefore, the expression for Δ presented in Eq. (1) and used elsewhere is now replaced by

$$\Delta = \mu_B(gB_z + g_{xz}B_x). \quad (9)$$

Note that the off-diagonal tensor component g_{xz} makes the magnetic response different for three orientations of $B_\parallel$: $B_\parallel = B_x$, $B_\parallel = -B_x$, and $B_\parallel = B_y$ [24]. This triples the amount of data we can get from the same sample. Details of our experimental setup/method are presented in Appendixes B, C, and D.

So far, we have only considered the effect of the external magnetic field, however, spin dynamics can also be influenced by additional couplings, such as the Rashba interaction (stemming from the asymmetry of the interface) and the Dresselhaus interaction (arising from the lack of inversion symmetry in the bulk GaAs crystal). We apply a voltage bias

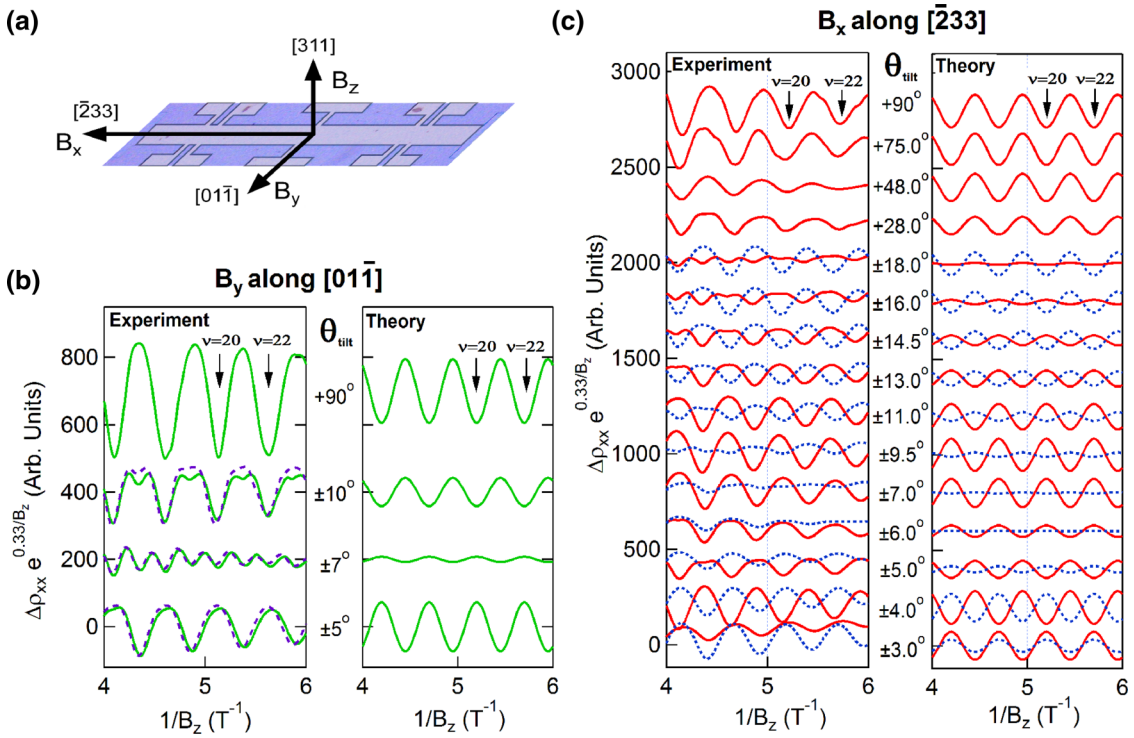

FIG. 2. Magnetoresistance (SdH) oscillations in an external magnetic field $\boldsymbol{B}$ applied at an angle $\theta_{\rm tilt}$ to the 2D heterostructure, $B_\parallel = B_z \tan\theta_{\rm tilt}$, $B_z > 0$. (a) The orientation of the magnetic field components relative to the crystal axes. (b) SdH oscillations plotted as a function of $\frac{1}{B_z}$ for an applied field of $B_y > 0$, $B_x = 0$ (green solid lines) and $B_y < 0$, $B_x = 0$ (purple dotted lines). Traces are offset for clarity. The amplitude of the oscillations was normalized by multiplying the data by $e^{0.33/B_z}$. SdH data are presented for the range in which the amplitude of the SdH oscillations is not too large ($\Delta\rho_{xx} < \rho_{xx}$) and B_z is small enough that we do not enter the quantum Hall regime (see Fig. 5). At $\theta_{\rm tilt} = \pm(7.0^\circ \pm 0.5^\circ)$ the oscillations exhibit an inversion corresponding to the change in sign of $\cos\Phi$ in Eq. (5). (c) SdH oscillations where the applied field is $B_x > 0$, $B_y = 0$ (red solid lines) and $B_x < 0$, $B_y = 0$ (blue dotted lines). Due to crystallographic anisotropy, the oscillations are distinctly different for different signs of B_x. In this orientation, the oscillations invert at angles $\theta_{\rm tilt} = 18^\circ \pm 1^\circ$, $5.5^\circ \pm 0.5^\circ$, $3.5^\circ \pm 0.25^\circ$ for $B_x > 0$ and $\theta_{\rm tilt} = -6.5^\circ \pm 0.5^\circ$ for $B_x < 0$. The filling factors ν are indicated by arrows at the tops of panels (b) and (c). The right-hand panels in (b) and (c) display theoretical SdH curves calculated using the non-Abelian theory and the usual Lifshitz-Kosevich formula, valid in the regime $\Delta\rho_{xx} \ll \rho_{xx}$.

to the back-gate, to tune the symmetry of the GaAs quantum well such that the Rashba interaction is practically zero (see Appendix D). The Dresselhaus interaction is relatively weak, nevertheless, it is important in some regimes. Moreover, as we discuss below, it brings an additional confirmation of the non-Abelian dynamics.

The results of our measurements are presented in Figs. 2(b) and 2(c) which plot resistivity versus $1/B_z$ where the in-plane field is altered by tilting the sample at an angle $\theta_{\rm tilt}$ with respect to the applied field, such that $B_z = B_\parallel \tan\theta_{\rm tilt}$, with $B_z > 0$. Figure 2(b) corresponds to tilting in the yz plane ($B_x = 0$) and Fig. 2(c) corresponds to tilting in the xz plane ($B_y = 0$). The data in Fig. 2(b) are symmetric with respect to $B_y \to -B_y$, while the data in Fig. 2(c) exhibit asymmetry with respect to $B_x \to -B_x$ due to nonvanishing g_{xz} in Eq. (9). According to Eqs. (5) and (7), the normalized amplitude of resistivity oscillations, $\cos\Phi$, is a function only of $\theta_{\rm tilt}$ and is independent of the magnitude of the total magnetic field $\boldsymbol{B}$. At tilt angles corresponding to changes in the sign of ${\rm tr}U = 2\cos\Phi$, the first harmonic of the SdH oscillations invert (i.e., maxima become minima, and vice versa). At these "coincidence" angles the phase Φ must coincide with a half-integer multiple of π. In the data, these coincidences are observed at the tilt angle $\theta_{\rm tilt} = \pm(7^\circ \pm 0.5^\circ)$ for the field applied along the yz plane in Fig. 2(b). For the field applied in the xz plane [Fig. 2(c)] there are multiple coincidence angles at $\theta_{\rm tilt} = 18^\circ \pm 1^\circ$, $5.5^\circ \pm 0.5^\circ$, $3.5^\circ \pm 0.25^\circ$ for $B_x > 0$ and only a single coincidence at $\theta_{\rm tilt} = -6.5^\circ \pm 0.5^\circ$ for $B_x < 0$. The coincidence angles are plotted in Fig. 3, and are described by Eqs. (7) and (9). There are three independent device-specific parameters in these equations, which are gm, $2\alpha k_F^2/(g\mu_B)$, and g_{xz}/g. We use the value $m = 0.25m_e$ derived in Appendix A as our reference point and hence we are left with unknowns g, $\lambda = 2\alpha k_F^2/\mu_B$, and g_{xz} which we treat as free fitting parameters.

Altogether we have three fitting parameters to describe five coincidence angles. To compare the experimental coincidence angles to those of theory, we perform a least-squares fit to Φ using the observed four coincidence angles for the orientations $B_x > 0, B_y = 0$ and $B_y \neq 0, B_x = 0$ [red and green symbols in Fig. 3(a)], and use the values obtained to predict the coincidence angles for the orientation $B_x < 0, B_y = 0$ [blue traces in Fig. 3(b)]. The solid red and green curves in Fig. 3(a) show the calculated Φ/π obtained from this fitting, with the following values of the fitting parameters: $g = 7$, $|\lambda| = 0.88$, and $g_{xz} = -0.87$. The solid blue line in Fig. 3(b) shows

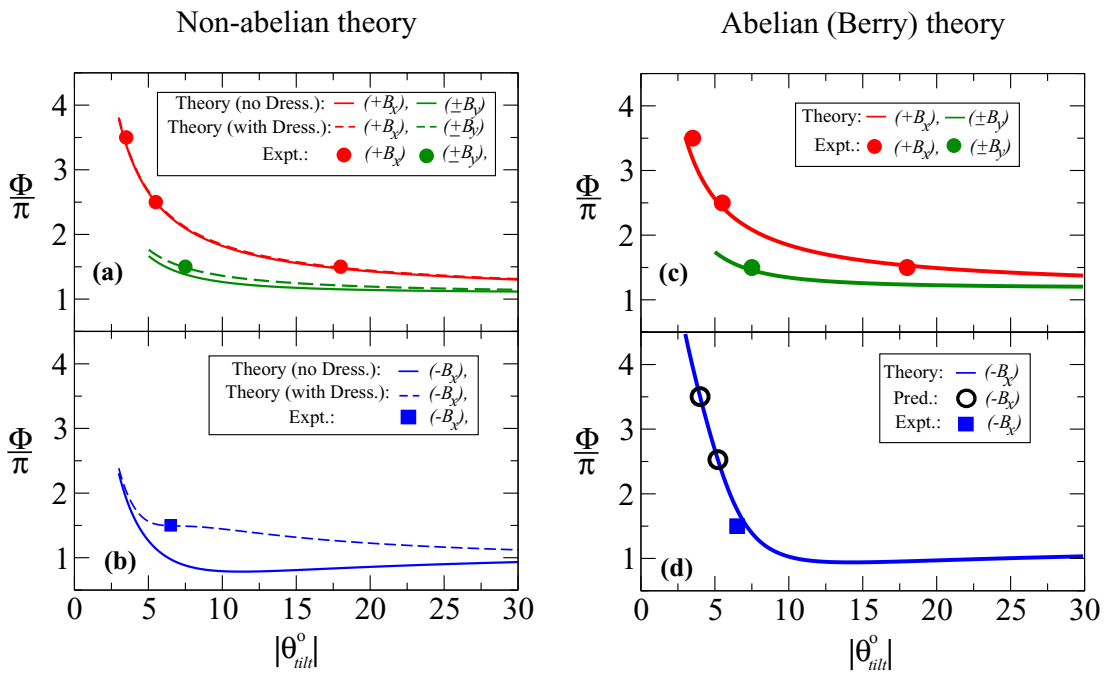

FIG. 3. Comparison of experimentally observed coincidences angles to the non-Abelian (a), (b) and Abelian (c), (d) theories. Expressing the envelope of the SdH oscillations as $\cos\Phi$, we find that Φ/π becomes a smooth function of tilt angle. This function is plotted for the experimental range of tilting angles. Angles at which Φ crosses a half-integer multiple of π correspond to inversions of the SdH oscillations. Both theories contain three unknown parameters g, g_{xz}, λ. In panels (a) and (c) we show the least-squares fits of Φ to the observed coincidence angles for an applied $B_x > 0, B_y = 0$ (red) and $B_y \neq 0, B_x = 0$ (green). The plots of Φ in panels (b) and (d) show the predicted coincidences for $B_x < 0, B_y = 0$. For the non-Abelian theory, the solid curves do not include the Dresselhaus perturbation, whereas it is included for the dashed curves. In the Abelian case, the influence of the Dresselhaus perturbation is negligible. The non-Abelian gauge theory predicts a single angle of coincidence blue solid line in panel (b), consistent with the observed coincidence point (blue square). Including the Dresselhaus interaction (blue dashed line) provides quantitative agreement with experiment. In contrast, the Abelian theory (d) predicts three coincidences while experimentally only one angle of coincidence was observed (solid blue square); the two coincidence angles marked with open symbols were not observed in experiment.

Φ/π for the $B_x < 0, B_y = 0$ orientation calculated using the fitting parameters from Fig. 3(a), which predicts that there will be only a single coincidence observed in the experimentally measured range of θ_{tilt}, in agreement with experiment (blue square). There is reasonable agreement between the predicted coincidence angle of $\theta_{\text{tilt}} = -4.5^\circ$ and that observed in the experiment of $\theta_{\text{tilt}} \approx -6.5^\circ \pm 0.5^\circ$, although we will shortly discuss the origins of this 2° discrepancy.

To highlight the non-Abelian dynamics, we have attempted to fit the observed data using the Abelian Berry formula (8) instead of Eq. (7). Using Eqs. (8) and (9), we repeat the same procedure described above and fit Φ_{AB} to the observed four coincidence angles for the orientations ($B_x > 0, B_y = 0$) and ($B_y \neq 0, B_x = 0$), as shown in Fig. 3(c). The fitting parameters obtained are $g = 9.5$, $|\lambda| = 0.54$, $g_{xz} = +0.81$. These parameters were then used to predict the coincidence angles occurring for the orientation $B_x < 0, B_y = 0$, shown in Fig. 3(d). The key point is that the Abelian theory always predicts three coincidence angles in contrast to the single coincidence observed in experiment.

Although the number of coincidence angles is not a topological invariant (for example, it depends on the range of tilt angles available in the experiment), it is robust within both the non-Abelian and the Abelian theories. As shown in Appendix E, although the precise tilt angles at which the coincidences occurred are sensitive to the fitting parameters, the *number* of coincidences could not be changed even after significant variation of the parameters.

Additional confirmation of the non-Abelian dynamics comes from the Dresselhaus interaction, neglected so far because of its smallness. In the corotating frame, the spin-orbit coupling given by Eq. (2) results in an energy splitting $\Delta_{\uparrow\downarrow} = \omega_c \frac{\Phi}{\pi}$ between the "up" and "down" spin states [see Eq. (7)]. The quantization axis for $\Delta_{\uparrow\downarrow}$ is tilted with respect to z. The Dresselhaus interaction in the corotating frame takes the form of a small periodic perturbation $\sigma_z \cos\omega_c t$. Since the quantization axis is tilted, this perturbation drives transitions between the spin "up" and spin "down." Because of the smallness of the perturbation, the transitions are significant only close to resonance $\Delta_{\uparrow\downarrow} \approx \omega_c$. We use the amplitude of the Dresselhaus interaction as an additional fitting parameter, and find that it is close to the value known from the literature (see Appendix F). The effect of the Dresselhaus perturbation is shown by the dashed curves in Figs. 3(a) and 3(b). The tiny difference from the red and green solid curves in Fig. 3(a), which do not include the Dresselhaus interaction, show that the effect of the interaction is very weak. On the other hand, for $B_x < 0$ [Fig. 3(b)] the resonance condition $\Delta_{\uparrow\downarrow} \approx \omega_c$ is satisfied and the Dresselhaus term now becomes significant. This causes a clear difference between the solid and dashed

blue curves in Fig. 3(b), which completely removes the small disagreement between experimental and theoretical values of the coincidence angle.

Of course, the inclusion of the Dresselhaus interaction does not influence the number of coincidence angles, which is a very robust number. Moreover, the inclusion of the Dresselhaus term explains why the single coincidence for $B_x < 0$ is not sharp, but occurs over a much wider range of angles than for $+B_x$ or $\pm B_y$ [seen as the slow phase inversion and small amplitude of the SdH oscillations in the range $5^\circ < |\theta_{\rm tilt}| < 10^\circ$ for blue traces in Fig. 2(b)]. This nonsharp transition for $B_x < 0$ is explained by the inflection in the blue dashed curve in Fig. 3(b), which is due to the Dresselhaus interaction. The "inflection" effect provides further confirmation of the non-Abelian dynamics since the small Dresselhaus perturbation is always insignificant in the Abelian theory.

Finally, we present in Figs. 2(b) and 2(c) theoretical SdH curves calculated with modified Lifshitz-Kosevich formula (5). The agreement between theory (including Dresselhaus interaction) and experiment is very good. Overall, our data on the number of coincidences, supported by the slow phase flip of the SdH oscillations for $B_x < 0$, provide unambiguous evidence for the non-Abelian gauge field.

The non-Abelian gauge field features centrally in theoretical proposals to exploit hole systems for spintronics and quantum information purposes, including the realization of the dissipationless spin Hall effect [12] and non-Abelian manipulation of hole qubits [25]. The capacity of hole systems in this context is further enhanced by the suppression of decoherence due to absence of the hyperfine interaction [26,27]. The observation of the non-Abelian gauge field in a 2D hole system has positive implications for future studies of hole systems which rely on this concept.

ACKNOWLEDGMENTS

We acknowledge B. Horowitz, U. Zuelicke, R. Winkler, and D. Miserev for important discussions. This work was supported by the Australian Research Council DP and DECRA schemes, and the EPSRC (UK).

APPENDIX A: DERIVATION OF THE SPIN-ORBIT INTERACTION FOR HEAVY HOLES

In a zinc-blende semiconductor, the hole wave function originates from atomic $p_{3/2}$ orbitals resulting in an angular momentum $J = \frac{3}{2}$. In the long-wavelength approximation, the effective Luttinger Hamiltonian for holes is quadratic in the hole momentum $\boldsymbol{k}$ [21] (see also Ref. [28]):

$$H_L = \left(\gamma_1 + \frac{5}{2}\gamma_2\right)\frac{\mathbf{k}^2}{2m_e} - \frac{\gamma_2}{m_e}\left(k_1^2 S_1^2 + k_2^2 S_2^2 + k_3^2 S_3^2\right) - \frac{\gamma_3}{m_e}(k_1 k_2\{S_1, S_2\} + k_2 k_3\{S_2, S_3\} + k_3 k_1\{S_3, S_1\}), \quad \text{(A1)}$$

1, 2, 3 are the crystal axes of the cubic lattice, m_e is the electron mass, $\{\ldots\}$ denotes the anticommutator, and γ_1, γ_2, and γ_3 are Luttinger parameters. In GaAs $\gamma_1 \approx 6.85$, $\gamma_2 \approx 2.1$, $\gamma_3 \approx 2.9$ [29]. The Hamiltonian (A1) can be rewritten as

$$H_L = \left(\gamma_1 + \frac{5}{2}\overline{\gamma}_2\right)\frac{\mathbf{k}^2}{2m} - \frac{\overline{\gamma}_2}{m}(\mathbf{k}\cdot\mathbf{S})^2 + k_i k_j S_m S_n T^{(4)}_{ijmn},$$

where

$$\overline{\gamma}_2 = \frac{2\gamma_2 + 3\gamma_3}{5} \approx 2.6.$$

The irreducible fourth-rank tensor $T^{(4)}_{ijmn}$ depends on the orientation of the cubic lattice, the tensor is proportional to $\gamma_3 - \gamma_2$. Neglecting $\gamma_3 - \gamma_2$ compared to γ_2, the Luttinger Hamiltonian can be approximated by the following rotationally invariant (independent of the lattice orientation) Hamiltonian:

$$H_L \to H = \frac{\hbar^2}{2m_e}\left[\left(\gamma_1 + \frac{5}{2}\overline{\gamma}_2\right)k^2 - 2\overline{\gamma}_2(\boldsymbol{k}\cdot\boldsymbol{J})^2\right]. \quad \text{(A2)}$$

Due to the confining potential $V(z)$, motion perpendicular to the 2D plane of the heterostructure is quantized, leading to the formation of 2D subbands, where only the lowest subband occupied in the low-temperature experimental regime. Assuming a square well confining potential of width d we have $\langle k_z^2\rangle = \frac{\pi^2}{d^2}$. Since $\langle k_z^2\rangle \gg k_F^2$, we may expand $-(\boldsymbol{k}\cdot\boldsymbol{J})^2 = -k_z^2 J_z^2 + \ldots$, with the leading term becoming diagonal in a basis of states with J_z. Due to the sign of the interaction, states with $J_z = \pm\frac{3}{2}$ (heavy hole) are lower in energy, and the splitting between these and states with $J_z = \pm\frac{1}{2}$ (light hole) at $k_x = k_y = 0$ becomes

$$\Delta_{hl} = 2\overline{\gamma}_2\frac{\pi^2\hbar^2}{m_e d^2} \approx 9.6 \text{ meV}. \quad \text{(A3)}$$

Here, we take $d = 20$ nm. The splitting between the lowest and the next heavy hole band at $k_x = k_y = 0$ is

$$\Delta_{h12} = \frac{3}{2}(\gamma_1 - 2\overline{\gamma}_2)\frac{\pi^2\hbar^2}{m_e d^2} \approx 4.6 \text{ meV}. \quad \text{(A4)}$$

Numerical diagonalization of the full Luttinger Hamiltinian (A1) using the NEXTNANO++ package [30] gives the energy levels (2D dispersions) plotted in Fig. 4.

The HH1-HH2 splitting at $k_x = k_y = 0$ is pretty close to (A4) while the HH1-LH1 splitting in Fig. 4 is somewhat smaller than (A3) because of the $\sim(\gamma_3 - \gamma_2)$ tensor corrections. At hole density corresponding to our experiment, $n \approx 10^{11}$ cm^{-2}, only the lowest band is populated. The lowest-band dispersion $\epsilon(\boldsymbol{k})$ enters Eq. (1). We describe this band by the effective spin $s = \frac{1}{2}$, $|J_z = +\frac{3}{2}\rangle \equiv |\uparrow\rangle$, $|J_z = -\frac{3}{2}\rangle \equiv |\downarrow\rangle$. The Fermi momentum is $k_F \approx 0.0079$ Å^{-1} and the Fermi energy $E_F \approx 1.3$ meV, is shown in Fig. 4 by the red horizontal line. The heavy-hole effective mass $m = k\left(\frac{d\epsilon}{dk}\right)^{-1}$ follows from Fig. 4. At $k \to 0$, the mass is about $0.14m_e$ and at $k = k_F$ the mass is $m \approx 0.25m_e$. Obviously, only the latter mass is relevant to our analysis.

The off-diagonal part of $(\boldsymbol{k}\cdot\boldsymbol{J})^2$ in the Hamiltonian (A2), $(\boldsymbol{k}\cdot\boldsymbol{J})^2 \to \frac{1}{4}(k_- J_+ + k_+ J_-)^2$, leads to heavy- and light-hole mixing:

$$|\boldsymbol{k},\uparrow\rangle = \left[\left|+\frac{3}{2}\right\rangle + ak_+^2\left|-\frac{1}{2}\right\rangle\right]e^{i\boldsymbol{k}\cdot\boldsymbol{r}},$$
$$|\boldsymbol{k},\downarrow\rangle = \left[\left|-\frac{3}{2}\right\rangle + ak_-^2\left|+\frac{1}{2}\right\rangle\right]e^{i\boldsymbol{k}\cdot\boldsymbol{r}}, \quad \text{(A5)}$$
$$a = \frac{\sqrt{3}\gamma_2}{2m_e\Delta_{hl}} = \frac{\sqrt{3}}{4\langle k_z^2\rangle}.$$

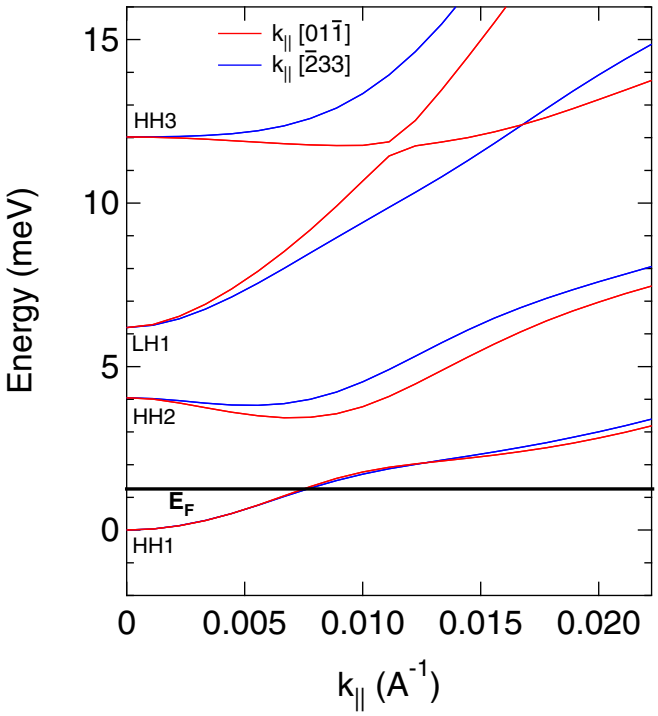

FIG. 4. Energy levels (2D dispersions) of holes in a (311) square quantum well of width $d = 20$ nm. The Fermi level shown by the red horizintal line, $E_F \approx 1.3$ meV, corresponds to the hole density $n = 10^{11}$ cm^{-2}.

Taking the square well width $d = 20$ nm and the hole density $n = 10^{11}$ cm^{-2}, we arrive at the following estimate for the mixing probability: $a^2k_F^4 = \frac{3}{4\pi^2}d^4n^2 \approx 1.2 \times 10^{-2}$. This very small mixing, of order 1% in probability, is responsible for the SOC considered here.

The Zeeman interaction of a $J = \frac{3}{2}$ hole with magnetic field $\boldsymbol{B}$ is [28]

$$\delta H = -\frac{g_0}{3}\mu_B \boldsymbol{B}\cdot\boldsymbol{J}, \tag{A6}$$

where $g_0 \approx 7.2$. Taking the matrix element of δH between states Eq. (A5) we find the effective matrix of $H_{\rm SOC}$:

$$\langle\downarrow|H_{\rm SOC}|\uparrow\rangle \equiv \langle\downarrow|\delta H|\uparrow\rangle = -\frac{g_0\mu_B}{4\langle k_z^2\rangle}B_+k_+^2. \tag{A7}$$

Comparing this with $H_{\rm SOC}$ in Eq. (1), we determine the coefficient α in this equation to be

$$\alpha = \frac{g_0\mu_B}{4\langle k_z^2\rangle}. \tag{A8}$$

According to our fit of SdH data $|\lambda| = 2|\alpha|k_F^2/\mu_B \approx 0.88$. Hence, we find that $k_F^2/k_z^2 \approx 0.25$ and the probability of the heavy- and light-hole mixing is $a^2k_F^4 = \frac{3}{16}\frac{k_F^4}{\langle k_z^2\rangle^2} \approx 1.1 \times 10^{-2}$, which is remarkably consistent with the estimate presented after Eq. (A5). It is worth noting that Eq. (A8) is approximate since one should expect a comparable contribution to α which is not accounted for by the calculations presented. So far, we have neglected the coupling to the vector potential created by $\boldsymbol{B}_\parallel$, $(\boldsymbol{k}\cdot\boldsymbol{J})^2 \to [(\boldsymbol{k} - e\boldsymbol{A})\cdot\boldsymbol{J}]^2$. This coupling also gives a contribution to the coefficient α (see Refs. [28,31]). This contribution is highly sensitive to the exact shape of the confining potential and therefore cannot be reliably calculated [31]. The kinematic form of $H_{\rm SOC}$, however, remains unambiguous and we can fit the value of α to the experimental data.

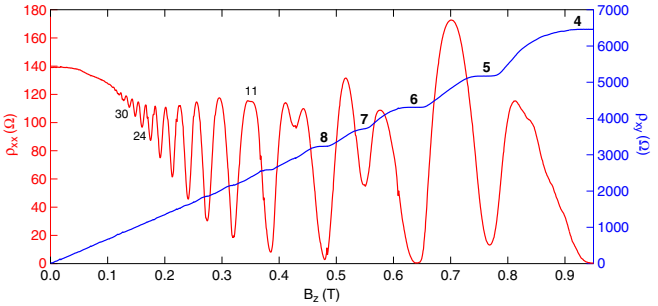

FIG. 5. Plot of SdH oscillations ρ_{xx} (in red) and corresponding Hall plateaus (in blue) as a function of perpendicular field B_z, taken at the symmetric operating point of $V_{BG} = +1.50$ V, where the 2D carrier density is $n = 9.26 \times 10^{10}$ cm^{-2} and the mobility 600 000 cm^2 V^{-1} s^{-1}.

APPENDIX B: SAMPLE AND TRANSPORT MEASUREMENTS

The 2D hole system resides within a symmetrically doped 20-nm-wide GaAs/$Al_{0.33}Ga_{0.67}$As quantum well, grown on the low-symmetry plane (311) by molecular beam epitaxy. A heavily doped n^+ GaAs layer located 2.6 μm below the quantum well, acts as an *in situ* back gate, allowing the 2D density to be tuned [32]. At zero back-gate voltage, the density of the 2D hole system is $n = 1.33 \times 10^{11}$ cm^2 with a corresponding mobility of $\mu = 678\,000$ cm^2 V^{-1} s^{-1}. Transport measurements were performed in a Kelvinox 100 dilution refrigerator within the bore of a 15-T magnet at a base temperature of 25 mK, using standard lock-in techniques, with a constant ac current of 10 nA at a frequency of 5 Hz. To perform tilted field measurements, the sample was mounted on a piezoelectric rotator which allowed for *in situ* rotation to be conducted with an accuracy of $\pm 0.01^\circ$ [33].

Initially the 2D device was rotated to $\theta_{\rm tilt} = 90^\circ$, so the magnetic field lies perpendicular to the sample plane, $B_z \neq 0$, $B_\parallel = 0$, and the sample orientation confirmed by measuring the Hall plateaus as a function of perpendicular field, shown in Fig. 5 (blue).

The corresponding low-field oscillating longitudinal resistivity is shown in (red), with spin-splitting appearing for $B_z > 0.35$ T. For the purposes of our analysis, we are only interested in low-field data between $B_z = 0.15$ and 0.25 T.

APPENDIX C: TILTED FIELD MEASUREMENTS

The coincidence method using tilted fields was first pioneered by Fang and Stiles in 1968 [34] to study the Landé g factor in 2D electron systems. Here, we perform a similar set of tilted field transport measurements for a 2D hole system, taken along two crystal directions: the high symmetry [0$\bar{1}$1] and the low symmetry [$\bar{2}$33], as depicted in Fig. 2(a). To achieve this, the device was first mounted on the rotator such that it tilts between the crystal axes [311] and [01$\bar{1}$], where the 2D plane is fully perpendicular to the field at $\theta_{\rm tilt} = 90^\circ$. The sample was then rotated towards the [0$\bar{1}$1] direction until

$\theta_{\text{tilt}} = +10^\circ$ to introduce a parallel field component B_y, and the total field $\boldsymbol{B}$ swept, changing the sign of the in-plane field $\pm B_y$. This procedure was repeated for a number of different $+\theta_{\text{tilt}}$ with increasing in-plane field components. The experiment was then repeated for equivalent $-\theta_{\text{tilt}}$ and the results plotted in Fig. 2(b). During a second cooldown, the sample was reoriented to perform tilted measurements along the [311] and low-symmetry [$\bar{2}$33] crystal axes. The experiment was then repeated for both $\pm\theta_{\text{tilt}}$ and the results shown in Fig. 2(c).

APPENDIX D: TUNING THE CONFINING POTENTIAL WITH THE BACK-GATE VOLTAGE TO COMPENSATE RASHBA SPIN-ORBIT INTERACTION

The electric potential across the quantum well was tuned via the *in situ* back gate, to adjust the confining potential. The presence of the Rashba SOC results in beatings of the SdH oscillations even without any tilting of the magnetic field [35]. The Rashba interaction is sensitive to the back-gate voltage (V_{BG}), so by varying the applied bias voltage, we can tune the system to minimize the amount of beatings and hence to eliminate the Rashba interaction. Figure 6 shows these beatings in detail, where the SdH oscillations at each back-gate voltage are periodic in $\frac{1}{B_z}$ and the amplitudes of these oscillations

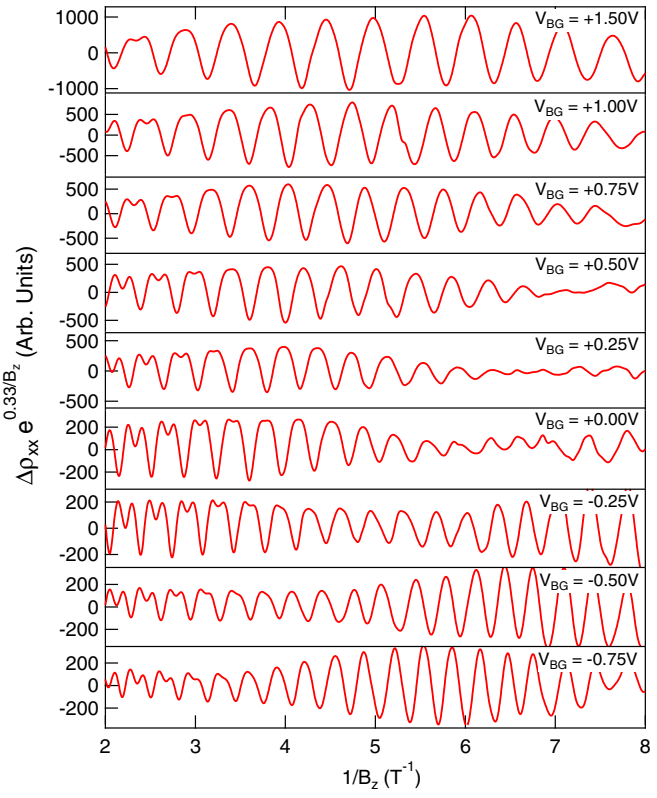

FIG. 6. Plots of the SdH oscillations ρ_{xx} periodic in inverse B_z, for different back-gate biases, with their amplitudes normalized by $e^{\frac{0.33T}{B_z}}$. The tilt angle $\theta_{\text{tilt}} = 90^\circ$, so $B_\parallel = 0$ T. In the top panel at $V_{BG} = +1.50$ V, the 2D carrier density is $n = 9.26 \times 10^{10}$ cm^2 and increases to $n = 1.53 \times 10^{11}$ cm^2 at $V_{BG} = -0.75$ V in the bottom panel. The back-gate voltage $V_{BG} = +1.50$ V produces SdH oscillations with the least beating and hence this was selected as the operating point for the rest of the experiment.

normalized for clarity by multiplying the data sets by $e^{\frac{0.33\,\text{T}}{B_z}}$ to remove the envelope.

The data are taken without any tilting, $\theta_{\text{tilt}} = 90^\circ$. From Fig. 6 we select $V_{BG} = +1.50$ V as the final operating point with the least amount of beating in the SdH oscillations. We will show that the major part of the Dresselhaus interaction does not influence dynamics at $\theta_{\text{tilt}} = 90^\circ$. Hence, minimizing the beating we tune the Rashba interaction to be close to zero. This back-gate voltage is used as the operating point for the rest of the experiment. At this point, the carrier density is $n = 9.26 \times 10^{10}$ cm^{-2} and the mobility is 600 000 cm^2 V^{-1} s^{-1}.

APPENDIX E: SENSITIVITY TO FITTING PARAMETERS

The comparison of the experimental result with possible theories is presented in Fig. 3. Figures 3(a) and 3(b) show the non-Abelian theory and Figs. 3(c) and 3(d) show the Abelian theory. The non-Abelian theory is consistent with experiment while the Abelian theory is not consistent. Since the conclusions are based on our fits, a natural question which arises is as follows: How sensitive is the number of coincidences with respect to variation in our fitting parameters? In Fig. 7, we show the response of the non-Abelian prediction Eq. (7) as the fitting parameters are varied.

The layout and color scheme are similar to Fig. 3: the top panels show the theoretical phase and the experimental

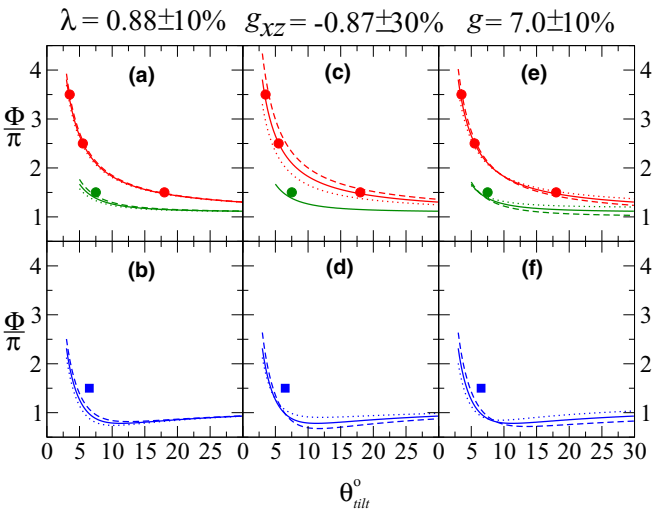

FIG. 7. Comparison of the non-Abelian theory (without accounting for the Dresselhaus interaction) with experiment. The plot Φ/π [defined by the envelope of the resistivity oscillations $\rho_{xx} \propto \cos\Phi$, see Eq. (7)] as a function of tilt angle for varied parameters λ, g_{xz}, g. The top panels show the phase and the experimental coincidence points for orientations of the external field $B_x > 0, B_y = 0$ (red) and $B_y \neq 0, B_x = 0$ (green). The bottom panels show the phase and the experimental coincidence points for the field orientation $B_x < 0, B_y = 0$ (blue). Experimentally observed coincidence angles are shown in symbols. Solid lines correspond to $\lambda = 0.88$, $g_{xz} = -0.87$, $g = 7.0$, and are identical to solid lines in Figs. 3(a) and 3(b). Dashed and dotted lines correspond to variations in λ by 10% [(a), (b)], g_{xz} by $\pm 30\%$ [(c), (d)], and g by $\pm 10\%$ [(e), (f)]. Note there is only one green line in panel (c) since at $B_y \neq 0, B_x = 0$ the phase is independent of g_{xz}.

coincidence points for orientations of the external field $B_x > 0, B_y = 0$ (red) and $B_y \neq 0, B_x = 0$ (green). The bottom panels show the phase and the experimental coincidence points for the field orientation $B_x < 0, B_y = 0$ (blue). Solid lines in Fig. 7 are identical to that in Figs. 3(a) and 3(b). Figures 7(a) and 7(b) correspond to ±10% variation of λ, Figs. 7(c) and 7(d) correspond to ±30% variation of g_{xz}, and Figs. 7(e) and 7(f) correspond to ±10% variation of g. From these plots, the presented deviations are larger than those accepted in Fig. 3. The curves corresponding to the lower boundaries of the parameters (dotted lines) are too far away from the experimental points. On the other hand, the curves corresponding to the upper boundaries of the parameters (dashed lines) demonstrate an additional coincidence point [Figs. 7(b), 7(d), 7(f)] which is not observed experimentally. This shows that the selected parameters $|\lambda| = 0.88$, $g_{xz} = -0.87$, $g = 7.0$ provide the best fit to the data. The curves in Fig. 7 do not account for the Dresselhaus interaction. There is no point to account for the interaction for purposes of the present analysis since it hardly affects the red and green curves which are used to determine the fit parameters, and it does not change the number of coincidences. Dresselhaus only deforms the blue curves in Figs. 7(b), 7(d), and 7(f) exactly in the same way as in Fig. 3(b).

A similar comparison for the Abelian theory [Eq. (8)] is presented in Fig. 8, where once again the parameters

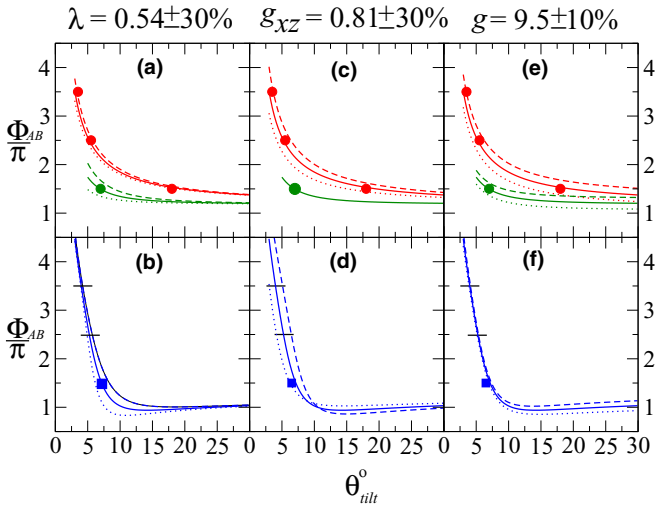

FIG. 8. Comparison of the Abelian theory with experiment. The plot Φ_{AB}/π [defined by the envelope of the resistivity oscillations $\rho_{xx} \propto \cos\Phi$, see Eq. (8)] as a function of tilt angle for varied parameters λ, g_{xz}, g. The top panels show the phase and the experimental coincidence points for orientations of the external field $B_x > 0, B_y = 0$ (red) and $B_y \neq 0, B_x = 0$ (green). The bottom panels show the phase and the experimental coincidence points for the field orientation $B_x < 0, B_y = 0$ (blue). Experimentally observed coincidence angles are shown in symbols. Solid lines correspond to $\lambda = 0.54, g_{xz} = 0.81, 9 = 9.5$, and are identical to the solid lines in Figs. 3(c) and 3(d). Dashed and dotted lines correspond to variation λ by 30% [(a), (b)], g_{xz} by ±30% [(c), (d)], and g by ±10% [(e), (f)]. The unobserved coincidences are shown in panels (b), (d), (f) by short black horizontal lines. There is only one green line in (c) since at $B_y \neq 0, B_x = 0$ the phase is independent of g_{xz}.

λ, g_{xz}, m are varied. The top panels show the theoretical phase Φ_{AB} and the experimental coincidence angles for orientations of the external field $B_x > 0, B_y = 0$ (red) and $B_y \neq 0, B_x = 0$ (green). The bottom panels show the phase and the experimental coincidence points for the field orientation $B_x < 0, B_y = 0$ (blue). Solid lines in Fig. 8 are identical to those in Figs. 3(c) and 3(d).

Figures 8(a) and 8(b) correspond to ±30% variation of λ, Figs. 8(c) and 8(d) correspond to ±30% variation of g_{xz}, and Figs. 8(e) and 8(f) correspond to ±10% variation of g. Despite the significant amount of variation in these parameters, the Abelian theory always predicts three coincidence angles for $B_x < 0, B_y = 0$ (blue), while experimentally only one angle is observed. This discrepancy illustrates that the experimental data cannot be reconciled with the paradigm of Berry phases alone and renders our evidence for the non-Abelian gauge field unambiguous.

APPENDIX F: ACCOUNTING FOR THE DRESSELHAUS INTERACTION

Dresselhaus spin-orbit interaction arises due to the lack of inversion symmetry in the bulk GaAs crystal. The interaction is cubic in the momentum k and linear in the angular momentum J (see Ref. [28]). In the coordinate system defined in Fig. 2(a), the leading term of the Dresselhaus Hamiltonian is

$$H_D \to -\frac{12\sqrt{22}}{121} b_D \langle k_z^2 \rangle k_y \sigma_z = -\frac{12\sqrt{22}}{121} b_D \langle k_z^2 \rangle k_F \sigma_z \sin\theta \,, \tag{F1}$$

where $b_D = 82$ eV Å^3 (see Ref. [28]). We neglect the subleading terms cubic in $k_\parallel$. The transformation (2) to the corotating frame does not change (F1). Hence, in the corotating frame the Dresselhaus interaction works as a weak periodic "magnetic field" superimposed on the constant "magnetic field" defined by Eq. (6). The projection of the periodic "field" on the direction perpendicular to the direction of the constant "field"

$$\sigma_z \sin\theta \to \sigma_\perp \frac{\alpha k_F^2 B_\parallel}{\sqrt{\left(\omega_c - \frac{\Delta}{2}\right)^2 + \left|\alpha k_F^2\right|^2 B_\parallel^2}} \sin\omega_c t \tag{F2}$$

generates spin flips. Accounting for the resonant part of the periodic perturbation, one finds that Φ given by Eq. (7) is replaced by Φ_D:

$$\frac{\Phi_D}{\pi} = 1 + \sqrt{\left(\frac{\Phi}{\pi} - 1\right)^2 + D^2},$$

$$D = D_0 \frac{\alpha k_F^2 B_\parallel}{\sqrt{\left(\omega_c - \frac{\Delta}{2}\right)^2 + \left|\alpha k_F^2\right|^2 B_\parallel^2}} \,, \tag{F3}$$

where

$$D_0 = \frac{12\sqrt{22}}{121} \frac{b_D \langle k_z^2 \rangle k_F}{\omega_c}. \tag{F4}$$

Without tilting, $\theta_{\rm tilt} = 90^\circ$, the Dresselhaus perturbation (F2) is zero, $\Phi_D = \Phi$. Hence, our back-gate tuning performed at $\theta_{\rm tilt} = 90^\circ$ does not compensate the Dresselhaus interaction. The interaction becomes important at intermediate values of $\theta_{\rm tilt}$. The dashed curves in Figs. 3(a) and 3(b) display Eq. (F3) calculated with $D_0 = 0.5$. We chose this value of D_0 to

shift the coincidence angle in Fig. 3(b) from $\theta_{\text{tilt}} = -4.5^\circ$ to $\theta_{\text{tilt}} \approx -6.5^\circ$. This is an additional fitting parameter. Because of weakness of the Dresselhaus interaction, the dashed and the solid curves in Fig. 3(a) are practically indistinguishable. On the other hand, because of the resonance, the effect of the Dresselhaus interaction in Fig. 3(b) is significant. We stress again the point made in the main text, the correct value of D_0 necessarily leads to the extended range of θ_{tilt} over which the phase of the SdH oscillation inverts, clearly seen in the blue traces in Fig. 2(c). The value of D_0 can be also calculated using Eq. (F4). With $B_z = 0.2$ T and with parameters of the system discussed in the paper, Eq. (F4) gives $D_0 \approx 0.8$. So, the Dresselhaus interaction is weak and insignificant compared to the dominating magnetic field controlled spin-orbit effects that drive the non-Abelian Berry phase. The strength of the Dresselhaus interaction measured in our experiment is slightly smaller but comparable with theoretical estimates presented in Refs. [28,36].

[1] C. N. Yang and R. L. Mills, Phys. Rev. **96**, 191 (1954).
[2] S. L. Glashow, Nucl. Phys. **22**, 579 (1961).
[3] M. V. Berry, Proc. R. Soc. London, Ser. A **392**, 45 (1984).
[4] F. Wilczek and A. Zee, Phys. Rev. Lett. **52**, 2111 (1984).
[5] A. Tomita and R. Y. Chiao, Phys. Rev. Lett. **57**, 937 (1986).
[6] J.-B. Yau, E. P. De Poortere, and M. Shayegan, Phys. Rev. Lett. **88**, 146801 (2002).
[7] B. Grbić, R. Leturcq, T. Ihn, K. Ensslin, D. Reuter, and A. D. Wieck, Phys. Rev. Lett. **99**, 176803 (2007).
[8] Y.-J. Lin *et al.*, Nature (London) **462**, 628 (2009).
[9] J. W. Zwanziger, M. Koenig, and A. Pines, Phys. Rev. A **42**, 3107 (1990).
[10] G. Moore and N. Read, Nucl. Phys. B **360**, 362 (1991).
[11] D. P. Arovas and Y. Lyanda-Geller, Phys. Rev. B **57**, 12302 (1998).
[12] S. Murakami, N. Nagaosa, and S.-C. Zhang, Science **301**, 1348 (2003).
[13] P. A. Lee, N. Nagaosa, and X.-G. Wen, Rev. Mod. Phys. **78**, 17 (2006).
[14] J. Dalibard, F. Gerbier, G. Juzeliunas, and P. Ohberg, Rev. Mod. Phys. **83**, 1523 (2011).
[15] F. Gerbier, N. Goldman, and M. Lewenstein, J. Phys. B: At., Mol. Opt. Phys. **46**, 130201 (2013).
[16] G. Engels, J. Lange, Th. Schäpers, and H. Luth, Phys. Rev. B **55**, R1958(R) (1997).
[17] B. Grbić, R. Leturcq, T. Ihn, K. Ensslin, D. Reuter, and A. D. Wieck, Phys. Rev. B **77**, 125312 (2008).
[18] L. Onsager, Philos. Mag. **43**, 1006 (1952).
[19] K. S. Novoselov *et al.*, Nature (London) **438**, 197 (2005).
[20] J. G. Analytis *et al.*, Nat. Phys. **6**, 960 (2010).
[21] J. Luttinger and W. Kohn, Phys. Rev. **97**, 869 (1955).
[22] I. M. Lifshitz and L. M. Kosevich, Zh. Eksp. Teor. Fiz. **33**, 88 (1958) [Sov. Phys.–JETP **6**, 67 (1958)].
[23] L. L. Thomas, Nature (London) **117**, 514 (1926).
[24] L. A. Yeoh, A. Srinivasan, O. Klochan, R. Winkler, U. Zülicke, M. Y. Simmons, D. A. Ritchie, M. Pepper, and A. R. Hamilton, Phys. Rev. Lett. **113**, 236401 (2014).
[25] J. C. Budich, D. G. Rothe, E. M. Hankiewicz, and B. Trauzettel, Phys. Rev. B **85**, 205425 (2012).
[26] Z. K. Keane *et al.*, Nano Lett. **11**, 3147 (2011).
[27] E. A. Chekhovich *et al.*, Nat. Mater. **12**, 494 (2013).
[28] R. Winkler, *Spin-Orbit Coupling Effects in Two-Dimensional Electron and Hole Systems* (Springer, Berlin, 2003), p. 212, 220.
[29] I. Vurgaftman, J. R. Meyer, and L. R. Ram-Mohan, J. Appl. Phys. **89**, 5815 (2001).
[30] S. Birner *et al.*, IEEE Trans. Electron Devices **54**, 2137 (2007).
[31] Y. Komijani *et al.*, Europhys. Lett. **102**, 37002 (2013).
[32] M. Y. Simmons *et al.*, Appl. Phys. Lett. **70**, 2750 (1997).
[33] L. A. Yeoh *et al.*, Rev. Sci. Instrum. **81**, 113905 (2010).
[34] F. F. Fang and P. J. Stiles, Phys. Rev. **174**, 823 (1968).
[35] J. P. Eisenstein, H. L. Stormer, V. Narayanamurti, A. C. Gossard, and W. Wiegmann, Phys. Rev. Lett. **53**, 2579 (1984).
[36] M. V. Durnev, M. M. Glazov, and E. L. Ivchenko, Phys. Rev. B **89**, 075430 (2014).